

Noise reduction in a laser polarimeter based on discrete waveplate rotations

Israel J. Vaughn and Brian G. Hoover

Advanced Optical Technologies, Albuquerque, NM, USA

hoover@advanced-optical.com

<http://www.advanced-optical.com>

Abstract: While several analyses of polarimeter noise-reduction have been published, little data has been presented to support the analytical results, particularly for a laser polarimeter based on measurements taken at discrete, independent rotation angles of two birefringent waveplates. This paper derives and experimentally demonstrates the reduction of both system and speckle noise in this type of laser polarimeter, achieved by optimizing the rotation angles of the waveplates by minimizing the condition numbers of the appropriate matrix equation. Results are demonstrated experimentally in signal-to-noise ratio (SNR) variations for a range of materials and spatial bandwidths. Use of optimal waveplate angles is found to improve the average SNR of the normalized Mueller matrix over speckle by a factor of up to 8 for a non-depolarizing material, but to provide little improvement for a depolarizing material. In the limit of zero spatial bandwidth, the average SNR of the normalized Mueller matrix over speckle is found to be greater than one for a non-depolarizing material and less than one for a depolarizing material.

© 2008 Optical Society of America

OCIS codes: (120.0280) Remote sensing and sensors; (120.5410) Polarimetry; (030.6140) Speckle

References and links

1. D. B. Chenault, J. L. Pezzaniti, and R. A. Chipman, "Mueller matrix algorithms," in *Polarization Analysis and Measurement*, D. Goldstein and R. Chipman, eds., Proc. SPIE **1746**, 231-246 (1992).
2. R. A. Chipman, "Polarimetry," in *Handbook of Optics*, (McGraw-Hill, New York, 1994), Chap. 22.
3. S. Breugnot and P. Clemenceau, "Modeling and performances of a polarization active imager at $\lambda = 806nm$," *Opt. Eng.* **39**, 2681-2688 (2000).
4. A. Ambirajan and D. C. Look, "Optimum angles for a polarimeter: part 1," *Opt. Eng.* **34**, 1651-1655 (1995).
5. J. Zallat, S. Aïnouz, and M. Ph. Stoll, "Optimal configurations for imaging polarimeters: impact of image noise and systematic errors," *J. Opt. A* **8**, 807-814 (2006).
6. Y. Takakura and J. E. Ahmad, "Noise distribution of Mueller matrices retrieved with active rotating polarimeters," *Appl. Opt.* **46**, 7354-7364 (2007)
7. M. H. Smith, "Optimization of a dual-rotating-retarder Mueller matrix polarimeter" *Appl. Opt.* **41**, 2488-2493 (2002)
8. R. M. A. Azzam, "Photopolarimetric measurement of the Mueller matrix by Fourier analysis of a single detected signal," *Opt. Lett.* **2**, 148-150 (1977)
9. J. W. Goodman, "Statistical properties of laser speckle patterns," in *Laser Speckle and Related Phenomena*, J. C. Dainty, ed., (Springer-Verlag, New York, 1984), Chap. 2.
10. E. Isaacson and H. B. Keller, *Analysis of Numerical Methods* (John Wiley and Sons, 1966).
11. G. W. Stewart, *Introduction to Matrix Computations* (Academic Press, New York, 1973).
12. R. Kress, *Numerical Analysis* (Springer-Verlag, Berlin, 1998).

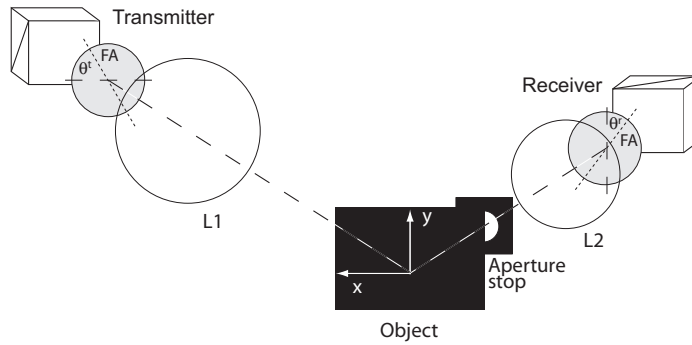
13. P. D. Lax, *Functional Analysis* (Wiley-Interscience, 2002).
14. D. S. Kliger, J. W. Lewis, and C. E. Randall, *Polarized Light in Optics and Spectroscopy* (Academic Press, 1990).
15. D. H. Goldstein and R. A. Chipman, "Error analysis of a Mueller matrix polarimeter," *J. Opt. Soc. Am. A* **7**, 693-700 (1990).
16. B. Boulbry, B. Le Jeune, F. Pellen, J. Cariou, and J. Lotrian, "Identification of error parameters and calibration of a double-crystal birefringent wave plate with a broadband spectral light source," *J. Phys. D* **35**, 2508-2515 (2002).
17. J. S. Tyo, "Design of optimal polarimeters: maximization of signal-to-noise ratio and minimization of systematic error," *Appl. Opt.* **41**, 619-630 (2002)
18. D. S. Sabatke, M. R. Descour, E. L. Dereniak, W. C. Sweatt, S. A. Kemme, and G. S. Phipps, "Optimization of retardance for a complete Stokes polarimeter," *Opt. Lett.* **25**, 802-804 (2000)
19. J. S. Tyo, "Noise equalization in Stokes parameter images obtained by use of variable-retardance polarimeters," *Opt. Lett.* **25**, 1198-1200 (2000).
20. B. G. Hoover, R. A. Peredo, L. F. DeSandre, and L. J. Ulibarri, "Active polarimetric assessment of surface weathering," in *Laser Radar Techniques for Atmospheric Sensing*, U. N. Singh, ed., Proc. SPIE **5575**, 38-43 (2004).
21. B. G. Hoover and J. S. Tyo, "Polarization components analysis for invariant discrimination," *Appl. Opt.* **46**, 8364-8373 (2007).
22. J. J. Gil, "Characteristic properties of Mueller matrices," *J. Opt. Soc. Am. A* **17**, 328-334 (2000).
23. J. J. Gil and E. Bernabeu, "A depolarization criterion in Mueller matrices," *Opt. Acta* **32**, 259-261 (1985).
24. J. J. Gil and E. Bernabeu, "Depolarization and polarization indices of an optical system," *Opt. Acta* **33**, 185-189 (1986).
25. M. Arioli, M. Baboulin, and S. Gratton, "A partial condition number for linear least squares problems," *SIAM J. Matrix Anal. Appl.* **29**, 413-433 (2007).

1. Introduction

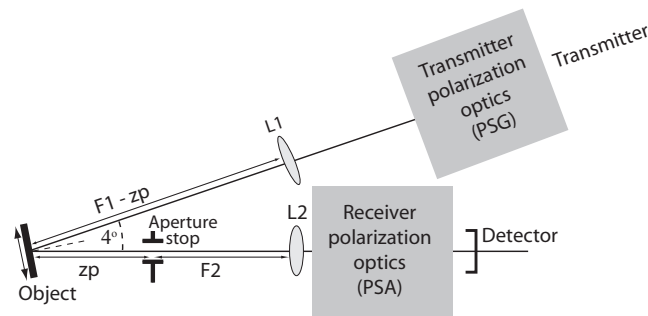
A well-known method for measurement of an object's Mueller matrix utilizes a polarized (typically laser) source, two polarizers (typically crossed linear analyzers), and two birefringent waveplates or retarders (typically quarter-wave retarders) in series with the object and an irradiance detector. Rotating the waveplates to 16 (or more) different combinations allows the Mueller matrix to be estimated from the corresponding irradiance measurements [1, 2, 3]. Illustrated in Fig. 1(a), this configuration is denoted a dual rotating-retarder (DRR) polarimeter.

As reviewed in Section 2.2 below, for this type of polarimeter the Mueller matrix is calculated as the product of the measured irradiance (or intensity) matrix \mathbf{I} and the inverses of the transmitter matrix \mathbf{T} and the receiver matrix \mathbf{R} [1, 2, 3]. The Mueller matrix can therefore be estimated using any transmitter and receiver configurations that correspond to non-singular matrices \mathbf{T} and \mathbf{R} , but the extent to which noise in \mathbf{I} (as well as in \mathbf{T} and \mathbf{R}) is amplified by the matrix inversions depends on the \mathbf{T} and \mathbf{R} configurations. Ambirajan and Look determined a set of waveplate angles that minimizes noise propagation in a Stokes polarimeter by finding the minimum condition numbers of the polarimeter matrix equation [4]. The optimization studied by Ambirajan and Look finds optimal angle sets for one of the waveplates (receiver) in the DRR polarimeter we seek to optimize. Several authors have presented analyses applicable to a *symmetric* DRR laser polarimeter, i.e., a polarimeter with the same transmitter and the receiver configurations [5, 6]. In Section 2 we generalize the analysis to a *non-symmetric* DRR polarimeter. Several optimal angle sets for this type of polarimeter are given in Section 3.1, and these are demonstrated experimentally in Section 3.2.

Since speckle is often the dominant noise source in a laser polarimeter, we first demonstrate noise reduction in the absence of speckle variation in Section 3.2.3.1, using a static object, and then demonstrate noise reduction in the presence of speckle variation in Section 3.2.3.2. Sources of non-speckle noise may include laser fluctuations, photon shot noise, detector electrical noise, random rotational errors, and other effects, although these are not resolved here but are lumped together as *system* noise. Speckle noise is realized by translating statistically-stationary objects in the xy -plane of Fig. 1 at a variety of receiver spatial bandwidths. The



(a)



(b)

Fig. 1. Schematic of the DRR polarimeter. (a) View from behind the object, with “FA” denoting the fast axes of the waveplates. (b) Top view, with PSG = polarization-state generator, PSA = polarization-state analyzer, $z_p = 290\text{mm}$, and $F_1 = 1\text{m}$, $F_2 = 350\text{mm}$ the focal lengths of lenses L1 and L2. The aperture stop is a variable iris.

objects or *materials* used for this paper are all planar coupons with (approximately) stationary statistics in the xy -plane. The telecentric system used to control the receiver bandwidth is illustrated in Fig. 1(b).

To our knowledge little data is available in the existing literature to support analyses of polarimeter noise reduction. An exception is Smith’s demonstration of noise reduction in an Azzam-type DRR polarimeter, [7] in which the transmitter and receiver waveplates rotate continuously with a variable velocity ratio [8]. Smith’s optimization assumes that the waveplate angles are equally spaced while the waveplate retardances are allowed to vary. Our analysis also allows the waveplate retardances to vary, although our experimental results are limited to variable, non-equally-spaced, non-symmetric waveplate rotation angles with the waveplate retardances fixed at nominally $\lambda/4$.

The experimental data presented in Section 3.2 supports our mathematical analysis of a DRR laser polarimeter with discrete waveplate rotation angles, demonstrating general improvement of the average signal-to-noise ratio (SNR) of the normalized Mueller matrix when using the derived optimal angle sets as opposed to traditional angle sets. The improvement against speckle noise in Mueller-averaged SNR is greater for non-depolarizing than for depolarizing materials.

Extrapolating speckle data to the limit of zero receiver bandwidth, i.e., a single speckle on the detector, we find that the Mueller-averaged SNR over speckle can be larger or smaller than the classical result (SNR = 1) for the polarized-intensity SNR over speckle, [9] depending on whether the material is non-depolarizing or depolarizing, respectively. This result is explained with reference to video of speckle patterns as seen through the modulated polarimeter.

2. Theory

2.1. Matrix norms and condition numbers

Matrix norms and condition numbers are utilized to derive the matrix error equation in Section 2.3. All norms $\|\cdot\|$ are positive definite, homogeneous, and satisfy the triangle inequality $\|\mathbf{A} + \mathbf{B}\| \leq \|\mathbf{A}\| + \|\mathbf{B}\|$; the norms we use also satisfy the consistency inequality $\|\mathbf{A}\mathbf{B}\| \leq \|\mathbf{A}\| \|\mathbf{B}\|$ [10, 11, 12]. A general functional derivation of operator norms can be found in Lax [13]. In Section 3 we use the 1-norm, 2-norm, ∞ -norm, and Frobenius-norm, respectively, on $\mathbb{R}^{4 \times 4}$ to quantify polarimeter measurement error due to noise:

$$\|\mathbf{A}\|_1 \stackrel{\text{def}}{=} \max_{1 \leq j \leq 4} \sum_{i=1}^4 |a_{ij}| \quad (2.1)$$

$$\|\mathbf{A}\|_2 \stackrel{\text{def}}{=} \sqrt{\lambda_{\max}(\mathbf{A}^* \mathbf{A})} \quad (2.2)$$

$$\|\mathbf{A}\|_{\infty} \stackrel{\text{def}}{=} \max_{1 \leq i \leq 4} \sum_{j=1}^4 |a_{ij}| \quad (2.3)$$

$$\|\mathbf{A}\|_{\text{Frob}} \stackrel{\text{def}}{=} \sqrt{\sum_{i=1}^4 \sum_{j=1}^4 |a_{ij}|^2}, \quad (2.4)$$

where a_{ij} is the element of \mathbf{A} at the i th row and j th column, $\lambda_{\max}(\mathbf{A})$ is the maximum eigenvalue of \mathbf{A} , and \mathbf{A}^* is the conjugate transpose of \mathbf{A} . The condition number is defined as

$$\kappa(\mathbf{A}) \stackrel{\text{def}}{=} \|\mathbf{A}\| \|\mathbf{A}^{-1}\| \quad (2.5)$$

for any matrix norm, such that $\kappa_1(\mathbf{A}) = \|\mathbf{A}\|_1 \|\mathbf{A}^{-1}\|_1$ for the 1-norm and analogously for the other norms. In Section 2.3 we use the following result from linear systems theory on the invertibility of a weakly-perturbed identity matrix (we use $\mathbf{1}$ to denote the identity matrix): if the norm of the perturbation \mathbf{P} is small, i.e. $\|\mathbf{P}\| < 1$, then $\mathbf{1} - \mathbf{P}$ is invertible and $\|(\mathbf{1} - \mathbf{P})^{-1}\| \leq (1 - \|\mathbf{P}\|)^{-1}$ [10, 11].

2.2. Matrix equation of DRR polarimeter

As illustrated in Fig. 1(a), the angle of rotation of the transmitter quarter-waveplate is denoted θ^t and that of the receiver quarter-waveplate is denoted θ^r . Using standard expressions for the Mueller matrices of the two quarter waveplates (\mathbf{M}_{qwp}) and ideal crossed linear polarizers

($\mathbf{M}_{p_0}, \mathbf{M}_{p_{90}}$) we obtain the DRR-polarimeter measurement equation [1, 2, 14]

$$\begin{aligned} \mathbf{S}_{out} &= \mathbf{M}_{p_0} \mathbf{M}_{qwp}(\theta^r) \mathbf{M} \mathbf{M}_{qwp}(\theta^t) \mathbf{M}_{p_{90}} \mathbf{S}_{in} \\ &= \frac{1}{4} \begin{bmatrix} 1 & \cos^2(2\theta^r) & \sin(4\theta^r)/2 & -\sin(2\theta^r) \\ 1 & \cos^2(2\theta^r) & \sin(4\theta^r)/2 & -\sin(2\theta^r) \\ 0 & 0 & 0 & 0 \\ 0 & 0 & 0 & 0 \end{bmatrix} \mathbf{M} \\ &\quad \times \begin{bmatrix} 1 & -1 & 0 & 0 \\ -\cos^2(2\theta^t) & \cos^2(2\theta^t) & 0 & 0 \\ -\sin(4\theta^t)/2 & \sin(4\theta^t)/2 & 0 & 0 \\ -\sin(2\theta^t) & \sin(2\theta^t) & 0 & 0 \end{bmatrix} \mathbf{S}_{in}, \end{aligned} \quad (2.6)$$

where the Mueller matrix of the object is denoted \mathbf{M} . With $\mathbf{S}_{in} = [1 \ -1 \ 0 \ 0]/\sqrt{2}$ and a narrow aperture stop in Fig. 1, the top row of Eq. 2.6 is the intensity measured by the polarimeter. If the intensity is measured for all combinations of angles (θ^t, θ^r) from the sets $\{\theta_1^t, \theta_2^t, \theta_3^t, \theta_4^t\}$ and $\{\theta_1^r, \theta_2^r, \theta_3^r, \theta_4^r\}$, which represent non-equally-spaced and non-symmetric discrete waveplate rotation angles, the matrix (data-reduction) equation can be developed as [1, 2, 3, 6]

$$\begin{aligned} \mathbf{I} &= \begin{bmatrix} 1 & \cos^2(2\theta_1^t) & \sin(4\theta_1^t)/2 & -\sin(2\theta_1^t) \\ 1 & \cos^2(2\theta_2^t) & \sin(4\theta_2^t)/2 & -\sin(2\theta_2^t) \\ 1 & \cos^2(2\theta_3^t) & \sin(4\theta_3^t)/2 & -\sin(2\theta_3^t) \\ 1 & \cos^2(2\theta_4^t) & \sin(4\theta_4^t)/2 & -\sin(2\theta_4^t) \end{bmatrix} \mathbf{M} \\ &\quad \times \begin{bmatrix} 1 & 1 & 1 & 1 \\ -\cos^2(2\theta_1^r) & -\cos^2(2\theta_2^r) & -\cos^2(2\theta_3^r) & -\cos^2(2\theta_4^r) \\ -\sin(4\theta_1^r)/2 & -\sin(4\theta_2^r)/2 & -\sin(4\theta_3^r)/2 & -\sin(4\theta_4^r)/2 \\ -\sin(2\theta_1^r) & -\sin(2\theta_2^r) & -\sin(2\theta_3^r) & -\sin(2\theta_4^r) \end{bmatrix} \\ &= \mathbf{RMT}, \end{aligned} \quad (2.7)$$

where \mathbf{I} is the intensity matrix containing the sixteen intensity measurements, and \mathbf{R} and \mathbf{T} are the receiver and transmitter measurement matrices, respectively. Inversion of the matrix equation (Eq. 2.7) provides an estimate of the Muller matrix of the object, \mathbf{M} . Zallat et. al. [5] express Eq. 2.7 using the Kronecker product.

A more general matrix equation for the DRR polarimeter can be obtained by allowing the waveplate phase retardances (denoted δ^t and δ^r) to differ from $\pi/2$ radians, i.e. we can allow the retardances of the waveplates to have arbitrary values. The generalized transmitter and receiver measurement matrices then become [2, 14]

$$\mathbf{T} = \begin{bmatrix} 1 & -\cos^2(2\theta_1^t) - \sin^2(2\theta_1^t) \cos \delta^t & -\sin(4\theta_1^t)(1 - \cos \delta^t)/2 & -\sin(2\theta_1^t) \sin \delta^t \\ 1 & -\cos^2(2\theta_2^t) - \sin^2(2\theta_2^t) \cos \delta^t & -\sin(4\theta_2^t)(1 - \cos \delta^t)/2 & -\sin(2\theta_2^t) \sin \delta^t \\ 1 & -\cos^2(2\theta_3^t) - \sin^2(2\theta_3^t) \cos \delta^t & -\sin(4\theta_3^t)(1 - \cos \delta^t)/2 & -\sin(2\theta_3^t) \sin \delta^t \\ 1 & -\cos^2(2\theta_4^t) - \sin^2(2\theta_4^t) \cos \delta^t & -\sin(4\theta_4^t)(1 - \cos \delta^t)/2 & -\sin(2\theta_4^t) \sin \delta^t \end{bmatrix}^T \quad (2.8)$$

and

$$\mathbf{R} = \begin{bmatrix} 1 & \cos^2(2\theta_1^r) + \sin^2(2\theta_1^r) \cos \delta^r & \sin(4\theta_1^r)(1 - \cos \delta^r)/2 & -\sin(2\theta_1^r) \sin \delta^r \\ 1 & \cos^2(2\theta_2^r) + \sin^2(2\theta_2^r) \cos \delta^r & \sin(4\theta_2^r)(1 - \cos \delta^r)/2 & -\sin(2\theta_2^r) \sin \delta^r \\ 1 & \cos^2(2\theta_3^r) + \sin^2(2\theta_3^r) \cos \delta^r & \sin(4\theta_3^r)(1 - \cos \delta^r)/2 & -\sin(2\theta_3^r) \sin \delta^r \\ 1 & \cos^2(2\theta_4^r) + \sin^2(2\theta_4^r) \cos \delta^r & \sin(4\theta_4^r)(1 - \cos \delta^r)/2 & -\sin(2\theta_4^r) \sin \delta^r \end{bmatrix}, \quad (2.9)$$

respectively.

2.3. Error equation of DRR polarimeter

Errors can be introduced in the measurements by errors in the rotation angles and/or the retardances of the quarter waveplates ($\Delta\mathbf{T}, \Delta\mathbf{R}$) or random fluctuations in the detected intensity ($\Delta\mathbf{I}$). Our analysis does not encompass errors due to imperfect optics, misalignment, or non-planar wavefronts [15, 16]. Consistent with Ambirajan and Look's error equation for a Stokes polarimeter, [4] Eq. 2.7 becomes the perturbed or error equation of the DRR polarimeter as

$$\mathbf{I} + \Delta\mathbf{I} = (\mathbf{R} + \Delta\mathbf{R})(\mathbf{M} + \Delta\mathbf{M})(\mathbf{T} + \Delta\mathbf{T}). \quad (2.10)$$

The minimization of $\|\Delta\mathbf{M}\|/\|\mathbf{M}\|$, the relative error in the Mueller-matrix estimate, will minimize the propagation of error and the amplification of variance in the estimate. Below we use Eq. 2.10 to derive a constraint on the relative error $\|\Delta\mathbf{M}\|/\|\mathbf{M}\|$. We denote the 4×4 identity matrix by $\mathbf{1}$. Matrix multiplication yields

$$\mathbf{R}^{-1}(\mathbf{I} + \Delta\mathbf{I})\mathbf{T}^{-1} = (\mathbf{1} + \mathbf{R}^{-1}\Delta\mathbf{R})\Delta\mathbf{M}(\mathbf{1} + \Delta\mathbf{T}\mathbf{T}^{-1}) + (\mathbf{1} + \mathbf{R}^{-1}\Delta\mathbf{R})\mathbf{M}(\mathbf{1} + \Delta\mathbf{T}\mathbf{T}^{-1}). \quad (2.11)$$

Noting that no element of \mathbf{R} or \mathbf{T} has an absolute value greater than 1, we assume that $\Delta\mathbf{R}$ and $\Delta\mathbf{T}$ are small enough such that

$$\|\mathbf{R}^{-1}\|\|\Delta\mathbf{R}\| < 1 \text{ and } \|\mathbf{T}^{-1}\|\|\Delta\mathbf{T}\| < 1. \quad (2.12)$$

In this case, according to the result on the invertibility of the perturbed identity matrix noted in Section 2.1, both $(\mathbf{1} + \mathbf{R}^{-1}\Delta\mathbf{R})$ and $(\mathbf{1} + \Delta\mathbf{T}\mathbf{T}^{-1})$ are invertible. Equation 2.11 then becomes

$$\begin{aligned} \Delta\mathbf{M} = & (\mathbf{1} + \mathbf{R}^{-1}\Delta\mathbf{R})^{-1} \left[\mathbf{R}^{-1}\Delta\mathbf{I}\mathbf{T}^{-1} - \mathbf{R}^{-1}\Delta\mathbf{R}\mathbf{M} \right. \\ & \left. - \mathbf{M}\Delta\mathbf{T}\mathbf{T}^{-1} - \mathbf{R}^{-1}\Delta\mathbf{R}\mathbf{M}\Delta\mathbf{T}\mathbf{T}^{-1} \right] (\mathbf{1} + \Delta\mathbf{T}\mathbf{T}^{-1})^{-1}, \end{aligned} \quad (2.13)$$

using the fact that $\mathbf{R}^{-1}\mathbf{I}\mathbf{T}^{-1} = \mathbf{M}$. Then by taking the norm and using the triangle and consistency inequalities we obtain

$$\begin{aligned} \|\Delta\mathbf{M}\| \leq & \|(\mathbf{1} + \mathbf{R}^{-1}\Delta\mathbf{R})^{-1}\| \left[\|\mathbf{R}^{-1}\|\|\Delta\mathbf{I}\|\|\mathbf{T}^{-1}\| + \|\mathbf{R}^{-1}\|\|\Delta\mathbf{R}\|\|\mathbf{M}\| + \|\mathbf{M}\|\|\Delta\mathbf{T}\|\|\mathbf{T}^{-1}\| \right. \\ & \left. + \|\mathbf{R}^{-1}\|\|\Delta\mathbf{R}\|\|\mathbf{M}\|\|\Delta\mathbf{T}\|\|\mathbf{T}^{-1}\| \right] \|(\mathbf{1} + \Delta\mathbf{T}\mathbf{T}^{-1})^{-1}\|. \end{aligned} \quad (2.14)$$

Again according to the invertibility theorem we have

$$\|(\mathbf{1} + \mathbf{R}^{-1}\Delta\mathbf{R})^{-1}\| \leq \frac{1}{1 - \|\mathbf{R}^{-1}\|\|\Delta\mathbf{R}\|} \text{ and } \|(\mathbf{1} + \Delta\mathbf{T}\mathbf{T}^{-1})^{-1}\| \leq \frac{1}{1 - \|\mathbf{T}^{-1}\|\|\Delta\mathbf{T}\|}, \quad (2.15)$$

which leads to

$$\begin{aligned} \|\Delta\mathbf{M}\| \leq & \frac{1}{h} \left[\|\mathbf{R}^{-1}\|\|\Delta\mathbf{I}\|\|\mathbf{T}^{-1}\| + \|\mathbf{R}^{-1}\|\|\Delta\mathbf{R}\|\|\mathbf{M}\| \right. \\ & \left. + \|\mathbf{M}\|\|\Delta\mathbf{T}\|\|\mathbf{T}^{-1}\| + \|\mathbf{R}^{-1}\|\|\Delta\mathbf{R}\|\|\mathbf{M}\|\|\Delta\mathbf{T}\|\|\mathbf{T}^{-1}\| \right], \end{aligned} \quad (2.16)$$

where we have defined

$$h \stackrel{\text{def}}{=} (1 - \|\mathbf{R}^{-1}\|\|\Delta\mathbf{R}\|)(1 - \|\mathbf{T}^{-1}\|\|\Delta\mathbf{T}\|) = \left(1 - \frac{\kappa(\mathbf{R})\|\Delta\mathbf{R}\|}{\|\mathbf{R}\|}\right) \left(1 - \frac{\kappa(\mathbf{T})\|\Delta\mathbf{T}\|}{\|\mathbf{T}\|}\right). \quad (2.17)$$

Dividing through by $\|\mathbf{M}\|$ and using the fact that

$$\|\mathbf{I}\| = \|\mathbf{RMT}\| \leq \|\mathbf{R}\|\|\mathbf{M}\|\|\mathbf{T}\| \quad (2.18)$$

$$\Rightarrow \frac{1}{\|\mathbf{M}\|} \leq \frac{\|\mathbf{R}\|\|\mathbf{T}\|}{\|\mathbf{I}\|}, \quad (2.19)$$

we obtain

$$\begin{aligned} \frac{\|\Delta\mathbf{M}\|}{\|\mathbf{M}\|} &\leq \frac{1}{h} \left[\frac{\kappa(\mathbf{R})\kappa(\mathbf{T})\|\Delta\mathbf{I}\|}{\|\mathbf{I}\|} + \|\mathbf{R}^{-1}\|\|\Delta\mathbf{R}\| + \|\Delta\mathbf{T}\|\|\mathbf{T}^{-1}\| + \|\mathbf{R}^{-1}\|\|\Delta\mathbf{R}\|\|\Delta\mathbf{T}\|\|\mathbf{T}^{-1}\| \right] \\ &= \frac{\kappa(\mathbf{R})\kappa(\mathbf{T})}{h} \left(\frac{\|\Delta\mathbf{I}\|}{\|\mathbf{I}\|} + \frac{\|\Delta\mathbf{R}\|\|\Delta\mathbf{T}\|}{\|\mathbf{R}\|\|\mathbf{T}\|} \right) + \frac{\kappa(\mathbf{T})}{h} \frac{\|\Delta\mathbf{T}\|}{\|\mathbf{T}\|} + \frac{\kappa(\mathbf{R})}{h} \frac{\|\Delta\mathbf{R}\|}{\|\mathbf{R}\|}, \end{aligned} \quad (2.20)$$

where

$$\kappa(\mathbf{A}) = \|\mathbf{A}^{-1}\|\|\mathbf{A}\|.$$

So we have derived the constraint

$$\boxed{\frac{\|\Delta\mathbf{M}\|}{\|\mathbf{M}\|} \leq \frac{\kappa(\mathbf{R})\kappa(\mathbf{T})}{h} \left(\frac{\|\Delta\mathbf{I}\|}{\|\mathbf{I}\|} + \frac{\|\Delta\mathbf{R}\|\|\Delta\mathbf{T}\|}{\|\mathbf{R}\|\|\mathbf{T}\|} \right) + \frac{\kappa(\mathbf{T})}{h} \frac{\|\Delta\mathbf{T}\|}{\|\mathbf{T}\|} + \frac{\kappa(\mathbf{R})}{h} \frac{\|\Delta\mathbf{R}\|}{\|\mathbf{R}\|}} \quad (2.21)$$

which is valid for all consistent norms if errors in the transmitter and receiver measurement matrices are sufficiently small according to Eq. 2.12. Clearly, if the condition numbers of both \mathbf{R} and \mathbf{T} are minimized, then the right-hand side of Eq. 2.21 is minimized, hence the left-hand side will be constrained.

This analysis provides a prescription for minimizing relative error and reducing noise in the DRR laser polarimeter by selection of waveplate parameters that minimize $\kappa(\mathbf{R})$ and $\kappa(\mathbf{T})$. If speckle is the dominant noise source, then the term in $\|\Delta\mathbf{I}\|$ dominates the right-hand side of Eq. 2.21, and the product $\kappa(\mathbf{R})\kappa(\mathbf{T})$ should be minimized. This condition has been noted previously and is related to the polarization states that constitute \mathbf{R} and \mathbf{T} forming regular tetrahedra on the Poincaré sphere [17].

3. Results

3.1. Optimal angle sets

The matrix equation Eq. 2.10 has unique solutions over $-\pi/2 \leq \theta_i' \leq \pi/2$ and $-\pi/2 \leq \theta_i'' \leq \pi/2$ for $1 \leq i \leq 4$, which restricts the optimization domain. Generally the condition numbers have many local minima. \mathbf{T} and \mathbf{R} also need to have 'large' determinants so that they are easily invertible. Using the norm definitions given in Eqs. 2.1-2.4, angle sets were obtained for the following optimizations:

- (a) Maximizing $(\det\mathbf{R})^2$ and $(\det\mathbf{T})^2$
- (b) Minimizing $\kappa_1(\mathbf{R})$ and $\kappa_1(\mathbf{T})$
- (c) Minimizing $\kappa_2(\mathbf{R})$ and $\kappa_2(\mathbf{T})$
- (d) Minimizing $\kappa_\infty(\mathbf{R})$ and $\kappa_\infty(\mathbf{T})$
- (e) Minimizing $\kappa_{\text{Frob}}(\mathbf{R})$ and $\kappa_{\text{Frob}}(\mathbf{T})$

Table 1. Optimum angle sets for a receiver quarter-waveplate (in degrees) under different optimizations.

Optimization	θ_1'	θ_2'	θ_3'	θ_4'	det	κ_1	κ_2	κ_∞	κ_{Frob}
det	-74.88	-38.31	74.88	38.31	1.49	8.56	3.40	7.76	6.43
det	-51.69	-15.12	15.12	51.69	1.49	8.55	3.40	7.76	6.43
κ_1	-77.02	-45.00	-12.98	45.00	1.27	7.56	4.09	6.71	6.87
κ_2	-50.56	-14.80	14.80	50.56	1.48	8.47	3.27	7.68	6.44
κ_∞	1.94	45.00	-29.91	-60.09	1.41	8.67	3.64	5.87	6.58
κ_∞	-45.00	-88.06	29.91	60.09	1.41	8.67	3.64	5.87	6.58
κ_{Frob}	-38.18	-75.63	38.13	75.56	1.48	8.44	3.34	7.51	6.42
κ_{Frob}	-14.54	14.27	-51.94	51.76	1.48	8.45	3.34	7.52	6.42
High κ	81.89	70.43	58.97	-78.54	0.032	185.37	86.51	93.71	96.33
22.5° angles	-22.50	0.00	22.50	45.00	0.50	21.66	10.35	15.31	13.57

Table 2. Optimum angle sets for a transmitter quarter-waveplate (in degrees) under different optimizations.

Optimization	θ_1'	θ_2'	θ_3'	θ_4'	det	κ_1	κ_2	κ_∞	κ_{Frob}
det	-51.69	-15.12	15.12	51.69	1.49	8.54	3.40	7.76	6.43
det	-74.88	74.88	38.31	-38.31	1.49	7.75	3.40	8.54	6.43
κ_1	1.94	45.00	-29.91	-60.09	1.41	5.87	3.64	8.67	6.58
κ_1	-45.00	-88.06	29.91	60.09	1.41	5.87	3.64	8.67	6.58
κ_2	-101.51	-72.10	-36.99	41.44	1.48	7.67	3.28	8.75	6.44
κ_∞	-77.02	-45.00	-12.98	45.00	1.27	6.71	4.09	7.57	6.87
κ_{Frob}	-38.18	-75.63	38.13	75.56	1.48	7.51	3.34	8.44	6.42
κ_{Frob}	-14.54	14.27	-51.94	51.76	1.48	7.52	3.34	8.45	6.42
High κ	81.89	70.43	58.97	-78.54	0.032	93.71	86.51	185.37	96.33
22.5° angles	22.50	0.00	-22.50	-45.00	0.50	15.31	10.35	21.66	13.57

In each case the extrema were located by searching the entire four-dimensional space with a step size of 0.1 radians and then applying a gradient-descent algorithm to find the local extrema for each θ_i' and θ_j' . The global extrema corresponding to each optimization were then found from all of the corresponding local extrema. This was accomplished using code developed in Matlab 7.

The angles calculated under each optimization are given in Tables 1 and 2. For condition-number optimizations there are typically multiplicities of different optimal angle sets, usually differing in sign or in different permutations of the same angles. We will not list them all here. Optimal angle sets used for the experimental demonstrations in Section 3.2 are given. Included in the tables are the calculated condition numbers under all five optimizations for each angle set. The condition numbers, obviously, are smaller than those when optimizing the angle set for maximum determinant, although the determinants for all optimized angle sets remain close to the maximum determinant over the four-dimensional parameter space. Using these optimal angle sets should make polarimeter measurements less sensitive to errors and noise. For comparison, also given in Tables 1 and 2 are angle sets that should perform particularly poorly (High κ), and a set of equally-spaced, symmetric angles (22.5° angles) that might correspond to a traditional, unoptimized polarimeter drive scheme. As is demonstrated in Section 3.2, under all optimizations considered these angle sets perform worse than the optimized sets, although

Table 3. Optimum angle sets for a receiver waveplate with arbitrary retardance (in degrees) under different optimizations.

Optimization	θ_1^r	θ_2^r	θ_3^r	θ_4^r	δ^r	\det	κ_1	κ_2	κ_∞	κ_{Frob}
κ_1	13.67	-45.34	44.90	76.57	134.10	2.65	5.47	2.16	3.96	4.83
κ_2	74.86	-38.33	-74.86	38.33	131.80	3.08	6.04	1.73	4.64	4.72
κ_∞	-1.95	-45.01	29.91	60.09	123.80	2.83	6.20	2.15	3.78	4.67
κ_{Frob}	14.97	-51.79	51.60	-15.27	-131.80	3.08	6.04	1.73	4.64	4.47

Table 4. Optimum angle sets for a transmitter waveplate with arbitrary retardance (in degrees) under different optimizations.

Optimization	θ_1^t	θ_2^t	θ_3^t	θ_4^t	δ^t	\det	κ_1	κ_2	κ_∞	κ_{Frob}
κ_1	88.05	-29.91	44.99	-60.09	123.80	2.83	3.78	2.15	6.20	4.67
κ_2	-51.68	15.13	-15.15	51.66	131.80	3.08	4.64	1.73	6.04	4.47
κ_∞	-13.56	-45.22	44.78	-76.43	133.99	2.66	3.96	2.15	5.44	4.83
κ_{Frob}	14.97	-51.79	51.60	-15.27	-131.80	3.08	4.64	1.73	6.04	4.47

against speckle noise the effects of optimization vary with the scattering characteristics of the material. In general, as demonstrated in Section 3.2, the reduction of speckle noise afforded by optimization (under any norm) is larger for non-depolarizing materials than for depolarizing materials.

We also optimized the transmitter and receiver matrices of Eqs. 2.8 and 2.9 with variable waveplate retardances. These results, shown in Tables 3 and 4, are not demonstrated experimentally, but they do agree with previously-published results [7, 18, 19].

3.2. Experimental demonstrations

3.2.1. Polarimeter

The polarimeter providing data supporting our noise-reduction analysis is shown schematically in Fig. 1. It is a custom-built instrument consisting of a rotating quartz retarder (nominal retardance = $\lambda/4$) and a fixed calcite polarizer in both the polarization-state generator (transmitter) and polarization-state analyzer (receiver), a cw helium-neon laser source of wavelength $\lambda = 632.8\text{nm}$ (Melles-Griot 25 LHP 925), and a silicon PIN photodiode detector (Newport 818-SL on Newport meter 2835-C). Background on this type of polarimeter is widely available, [2, 3] and details peculiar to our polarimeter have been previously published [20, 21] and will not be reiterated in depth here, except to note that all of the data presented in this paper was acquired in the quasi-monostatic configuration shown in Fig. 1, with a 4° angle between the transmitter and receiver axes and a 2° incident angle on the object. The telecentric system depicted in Fig. 1 produces a converging beam 3mm in diameter on the object. The spatial bandwidth can be controlled over the range $3.0 - 65.5\text{mm}^{-1}$ by manual adjustment of the variable aperture stop over the corresponding diameter range $0.56 - 12\text{mm}$.

3.2.2. Materials

Experimental data was collected for several test materials: black flat paint, green flat paint, rolled titanium, and Spectralon. These materials differ considerably in their polarization signatures, and particularly in their depolarization properties. The depolarization index defined by

Table 5. Test materials: measured depolarization indices and relative polarized intensities.

Material	Di	$(m_{00} + m_{11})/2$
Spectralon	0.037	8.05
Green flat paint	0.442	1.53
Titanium	0.984	111.4
Black flat paint	0.993	1

Gil and Bernabeu, [23, 24]

$$\text{Di}(\mathbf{M}) = \frac{1}{\sqrt{3}} \left\| \frac{\mathbf{M}}{m_{00}} - \mathbf{ID} \right\|_{\text{Frob}}, \quad (3.1)$$

is used to quantify the depolarization properties, where \mathbf{ID} is the Mueller matrix of an ideal depolarizer ($m_{00} = 1$ and all other elements equal zero). Note that $\text{Di} = 0$ for a perfect depolarizer. Table 5 gives the depolarization indices and the relative polarized intensities $(m_{00} + m_{11})/2$ of the test materials as measured by the polarimeter (using the 1-norm angle set of Tables 1 and 2). The relative polarized intensities are cited below in assessing the dependence of system noise on detected power.

3.2.3. Noise reduction

For each test material and configuration, 50-60 Mueller matrices were measured using each of the optimal angle sets given in Tables 1 and 2, an unoptimized 22.5° angle set, and, for some configurations, an angle set with high condition number in all norms. Each test material was measured in both a static configuration, with the material coupon fixed between matrix measurements (50 matrices acquired), and a speckle configuration, with the material coupon translated between matrix measurements in the xy -plane of Fig. 1 in order to change the detected speckle pattern (60 matrices acquired). Data acquired in the static configuration reveals the reduction of system noise, while that acquired in the speckle configuration reveals the reduction of combined system and speckle noise. The speckle data is further resolved according to spatial bandwidth as discussed below. The SNR of each element of each normalized Mueller matrix was then calculated over the 50-60 data realizations. After “vectorizing” the Mueller matrices as

$$\begin{bmatrix} m_0 & m_1 & \cdots & m_{14} & m_{15} \end{bmatrix} \equiv \begin{bmatrix} 1 & \frac{m_{01}}{m_{00}} & \cdots & \frac{m_{32}}{m_{00}} & \frac{m_{33}}{m_{00}} \end{bmatrix}, \quad (3.2)$$

we define the Mueller-averaged SNR of the normalized Mueller matrix as

$$\Sigma_{\mathbf{M}}(\mathbf{M}) \stackrel{\text{def}}{=} \frac{1}{15} \sum_{i=1}^{15} \frac{|\bar{m}_i|}{\sigma_i}, \quad (3.3)$$

where \bar{m}_i is the mean element and σ_i the standard deviation of that element over the 50-60 data realizations. $\Sigma_{\mathbf{M}}$, the Mueller-averaged SNR, is generally expected to increase with Di (Eq. 3.1) simply because the means $|\bar{m}_i|$ generally increase. The significant features of the following results are variations of Mueller-averaged SNR with the angle set and between the static and speckle configurations. Reduction of speckle noise is more effective as Di increases.

3.2.3.1. System noise

Here *system noise* is classified as any noise not due to speckle. This includes noise that can be modeled by $\Delta\mathbf{I}$ in Eqs. 2.10 and 2.21, like laser power or polarization fluctuations, photon shot

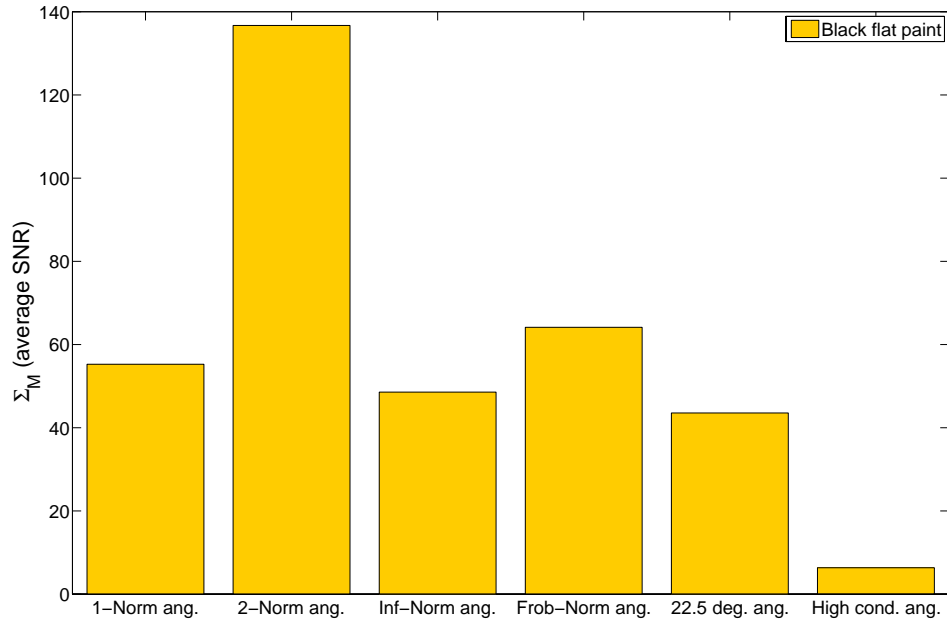


Fig. 2. Mueller-averaged SNR of the due to black flat paint measured in the static configuration using different waveplate-angle sets.

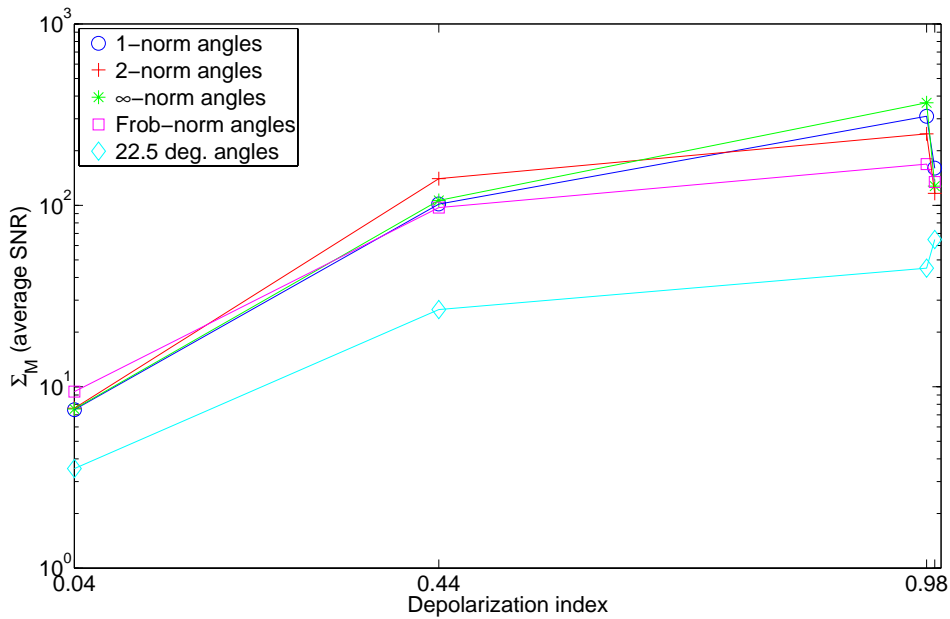


Fig. 3. Mueller-averaged SNR due to materials with different depolarization indices, measured in the static configuration using different waveplate-angle sets.

noise, and detector electrical noise, noise that can be modeled by $\Delta\mathbf{T}$ and $\Delta\mathbf{R}$, like waveplate-rotation errors, and possible noise sources that are not encompassed in the analysis of Section 2.3. We do not attempt to characterize system noise here, except to note that it is found to vary

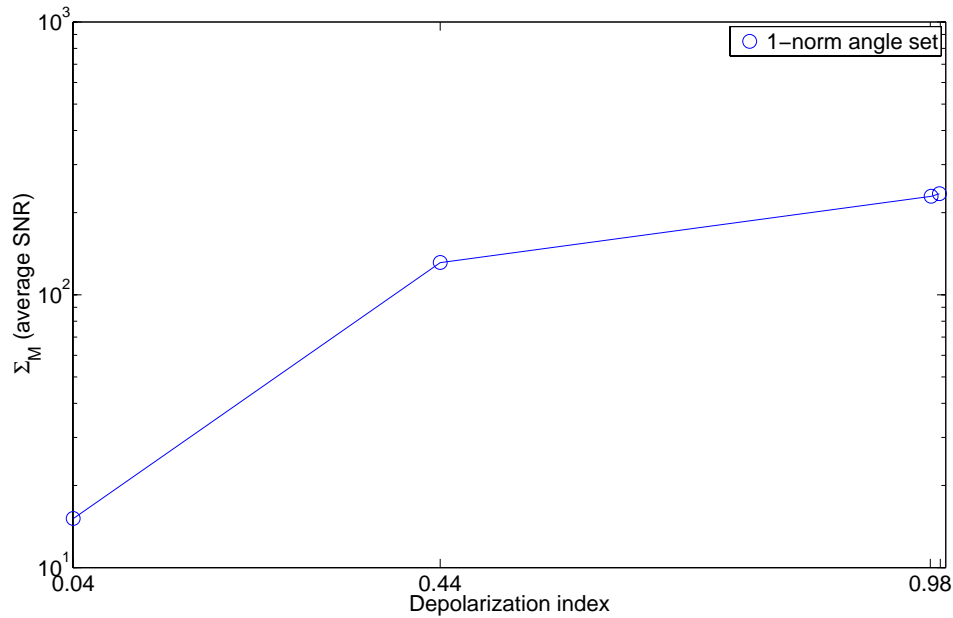
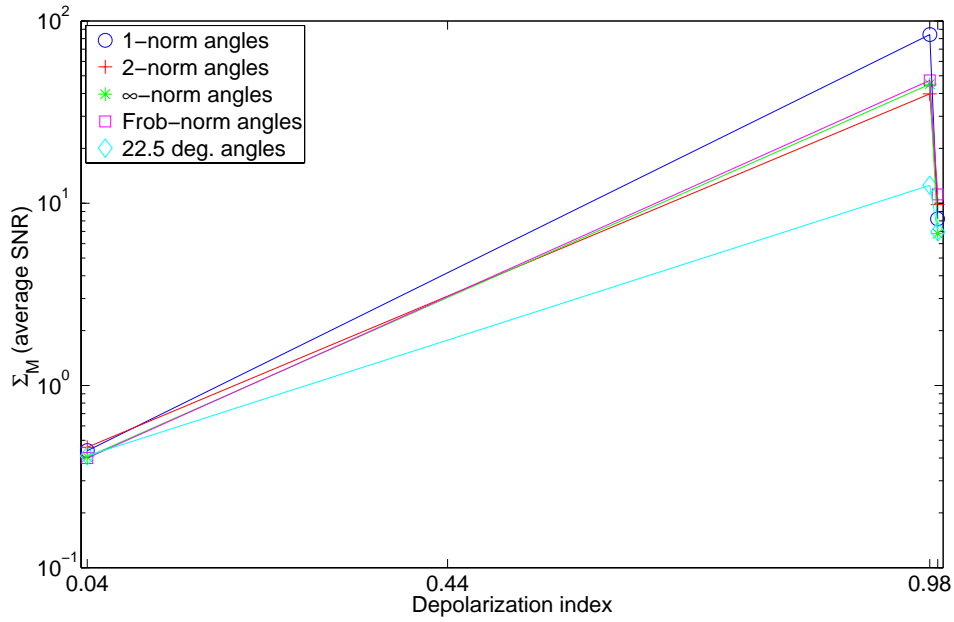


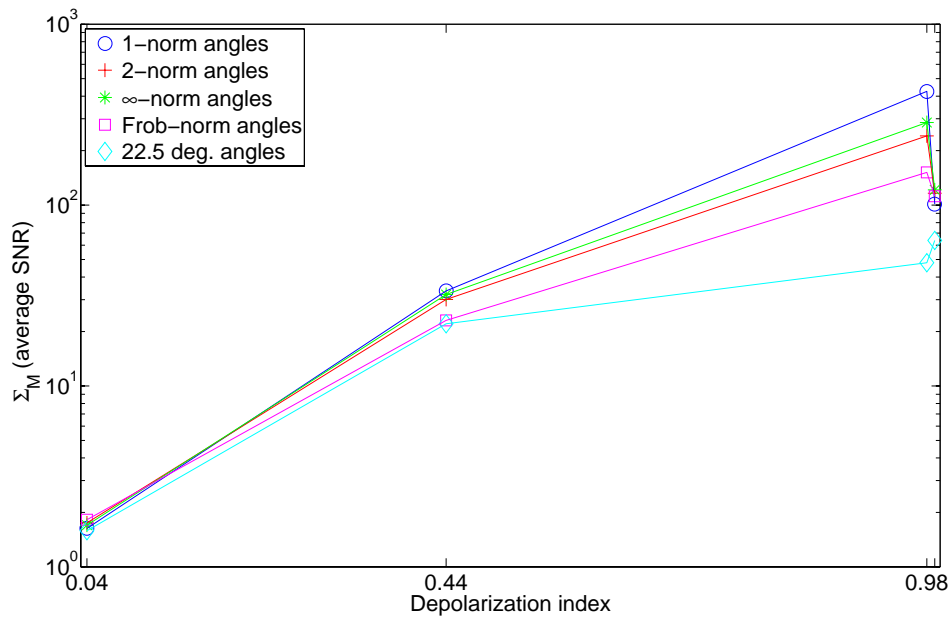
Fig. 4. Mueller-averaged SNR of the Mueller matrices due to materials with different depolarization indices, measured in the static configuration using the 1-norm angle set, with equalized power on the detector.

considerably from day to day, so that most of the data presented for comparisons among angle sets, materials, and/or spatial bandwidths was taken on the same day. Despite this uncertainty, data taken on the same day consistently show SNR improvements against system noise when optimal angle sets are used.

Figure 2 demonstrates improvements in the Mueller-averaged SNR due to black flat paint in data collected over multiple days. In this case the greatest improvement is achieved using the 2-norm angle set, a 209% improvement over the Mueller-averaged SNR using the 22.5° angle set. The ∞-norm angle set, however, provides only an 11% improvement over the 22.5° angle set. The Mueller-averaged SNR is much lower using the angle set with high condition number, demonstrating the error/noise amplification of an ill-conditioned system. The data shown in Fig. 3, which was all collected on the same day, suggests that the improvement achieved with the 2-norm angle set in Fig. 2 is more representative than that achieved with the other optimal angle sets. For the data in Fig. 3 the 22.5° angle set results in significantly lower Mueller-averaged SNR than any of the optimal angle sets, with improvements when using the optimal angle sets up to 126%, 319%, 507%, and 108% for Spectralon, green flat paint, titanium, and black flat paint, respectively. In Fig. 3 the Mueller-averaged SNR generally increases with the depolarization index (Eq. 3.1) as expected, and the optimal angles correspond to significant SNR improvement against system noise for all levels of depolarization. In the next section we show that this is not the case against speckle noise. The Mueller-averaged SNR drop between the titanium ($D_i = .984$) and the black flat paint ($D_i = .993$) seen in Fig. 3 is due to the corresponding 99% drop in detected power, which is quantified in Table 5. Figure 4 demonstrates the influence of detected power on system noise. For the data of Fig. 4 the detected intensity due to each material was equalized, to the level of the black flat paint, by means of a variable power attenuator in the transmitter. We cannot explain the increase in the Mueller-averaged SNR between the titanium and black flat paint with the 22.5° angle set in Fig. 3.



(a)



(b)

Fig. 5. Mueller-averaged SNR due to materials with different depolarization indices, measured using different waveplate-angle sets in the speckle configuration with a spatial bandwidth of (a) 3.0 mm^{-1} and (b) 65.5 mm^{-1} .

3.2.3.2. Speckle noise

Speckle noise is modeled by $\Delta\mathbf{I}$ in Eqs. 2.10 and 2.21. In order to examine the reduction of speckle noise, for each material and each angle set the following procedure was repeated

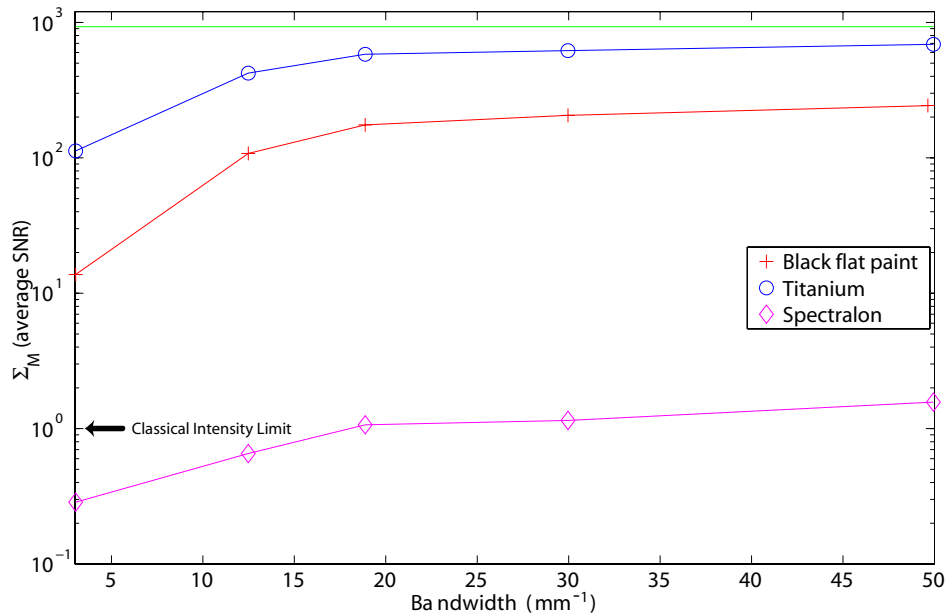


Fig. 6. Mueller-averaged SNR over speckle due to materials with different depolarization indices, measured using the 2-norm waveplate-angle set and variable spatial bandwidth. The green line at the top is the Mueller-averaged SNR over system noise of the titanium data. The theoretical result for polarized-intensity SNR over speckle in the limit of zero spatial bandwidth is annotated (the classical intensity limit).

5 times: an intensity matrix was measured and the material coupon then translated 5mm in the horizontal direction, which was repeated 12 times. Results are shown in Fig. 5 for low and high spatial bandwidths. All of the data in Fig. 5 was taken on the same day. As expected, the Mueller-averaged SNR increases with D_i and with the spatial bandwidth. The most significant feature of Fig. 5 may be that the Mueller-averaged SNR improvement against speckle using optimal angle sets is strongly dependent on the depolarization. Indeed, all of our speckle data imply that optimal waveplate-angle sets provide no significant improvement in the Mueller-averaged SNR against speckle if the material is, like Spectralon, highly depolarizing. Conversely, for non-depolarizing materials the optimal angle sets can provide significant improvements in the Mueller-averaged SNR against speckle as compared with the 22.5° angle set. For both bandwidths in Fig. 5 the largest improvement is seen for titanium, with the Mueller-averaged SNR achieved using the 1-norm angle set a considerable 786% improvement over the Mueller-averaged SNR achieved using the 22.5° angle set. For the titanium the optimal angle set achieving the least improvement, the Frobenius-norm set, still attains a Mueller-averaged SNR 216% over that of the 22.5° angle set. Whether the 1-norm angle set consistently outperforms the other optimal sets, as implied by Fig. 5, is a subject for future investigations.

We also found some interesting results for the variation of the Mueller-averaged SNR over speckle as a function of spatial bandwidth. All of this data was collected using the 2-norm angle set. The variable aperture stop illustrated in Fig. 1(b) controls the spatial bandwidth continuously over the range $3.0 - 65.5 \text{ mm}^{-1}$. At smaller bandwidths there are fewer speckles on the detector, so that speckle fluctuations or noise should be more pronounced as the material is translated. Referring to Eq. 2.21, $\|\Delta\mathbf{I}\|/\|\mathbf{I}\|$ therefore increases as the bandwidth decreases. This behavior is demonstrated in Fig. 6, for which all of the data for each material was collected

on the same day. As the bandwidth increases the Mueller-averaged SNR over speckle should approach the Mueller-averaged SNR over system noise, which for titanium is indicated by the green line along the top of Fig. 6 that represents the Mueller-averaged SNR due to titanium in the static configuration with the aperture stop open. For the data in Fig. 6 the power on the detector was not equalized—larger spatial bandwidths also imply more power—so the trend is a combination of power and bandwidth effects, although comparison of Fig. 6 with Figs. 3 and 4 confirms that speckle noise dominates the Mueller-averaged SNR in Fig. 6 at lower bandwidths.

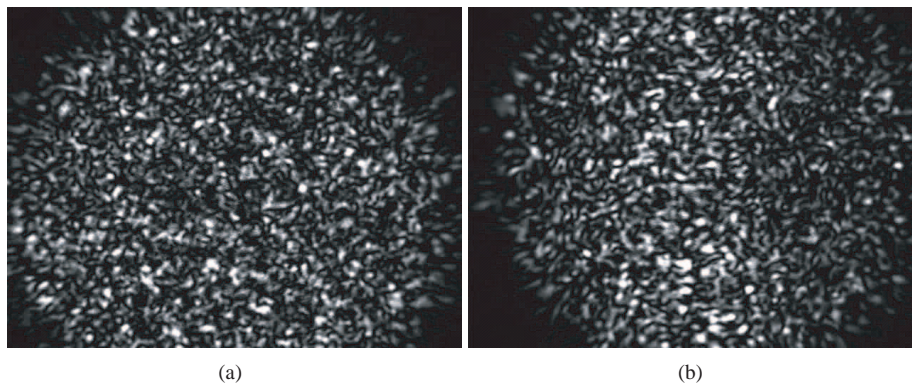
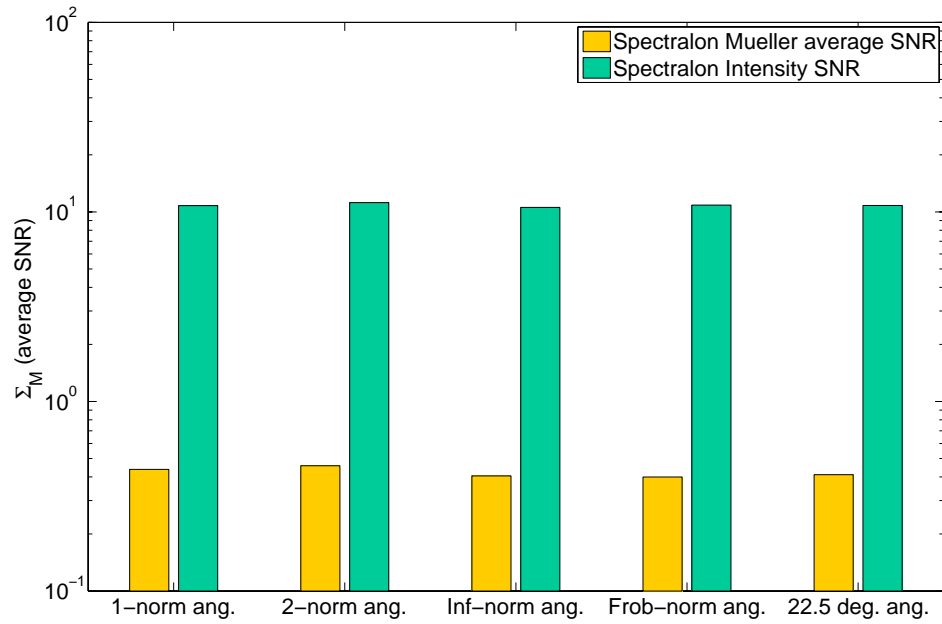


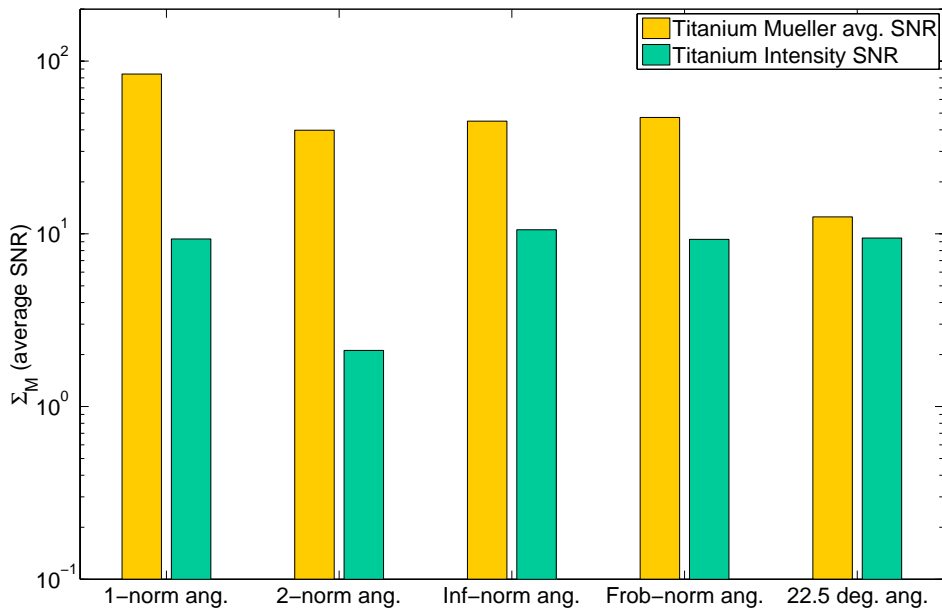
Fig. 7. Speckle patterns as seen through the modulated polarimeter due to (a) Spectralon (b) Titanium. Click on the pictures above to view the videos.

An interesting comparison afforded by Fig. 6 is that of the Mueller-averaged SNR over speckle with the polarized-intensity SNR over speckle in the limit of zero bandwidth. The theoretical limit of the polarized-intensity SNR over speckle is the well-known result $\text{SNR} = 1$, [9] which is annotated in Fig. 6. Extrapolating our results in Fig. 6 suggests that the limit of the Mueller-averaged SNR over speckle, defined by Eq. 3.3, can be greater than or less than one, depending on the depolarization of the material. To examine this effect more closely, from our data we calculated the polarized-intensity SNR over speckle and compared it to the Mueller-averaged SNR over speckle for depolarizing and non-depolarizing materials at low bandwidth. We used $(m_{00} + m_{11})/2$ for the polarized intensity. The remarkable results are shown in Fig. 8. For a depolarizing material Fig. 8(a) shows that the polarized-intensity SNR over speckle is more than an order of magnitude greater than the Mueller-averaged SNR over speckle at bandwidth 3mm^{-1} . As noted earlier, for a depolarizing material the SNR over speckle is not improved by using optimal waveplate angles. Figure 8(b) compares the speckle SNRs for a non-depolarizing material at the same bandwidth. The polarized-intensity SNR is approximately the same as for the depolarizing material, but the Mueller-averaged SNR is considerably larger, particularly with the optimal waveplate angles. This observation has broad implications for polarized sensors. It basically implies that, in terms of SNR, there is no justification for a full polarimetric measurement of a depolarizing material. Obviously, what is meant here by “depolarizing,” i.e., the value of D_i at which the Mueller-averaged SNR equals the polarized-intensity SNR, is a key question.

The results of Fig. 8 can be explained visually with reference to video of the speckle patterns as seen through the modulated polarimeter. For these videos a camera was dropped in front of the polarimeter detector in the configuration of Fig. 1, the spatial bandwidth was $\sim 30\text{mm}^{-1}$, and the ∞ -norm angles from Tables 1 and 2 were used. Polarization differences in the speckle patterns appear as irradiance differences as seen through the polarimeter. [Video 1](#) shows the



(a)



(b)

Fig. 8. Mueller-averaged SNR over speckle compared with polarized-intensity SNR over speckle at low bandwidth. (a) Spectralon/highly depolarizing and (b) Titanium/non-depolarizing.

speckle pattern due to Spectralon. Decorrelation of the speckle as the polarimeter waveplates rotate reveals that the speckle pattern is randomly-polarized over the detector/camera plane, as

we would expect. [Video 2](#) of the speckle pattern due to titanium is however fundamentally different. As the polarimeter waveplates rotate the titanium speckle pattern does not decorrelate, but rather varies in overall irradiance. We are led to conclude that, although the titanium produces a fully-developed speckle pattern, the speckle is almost uniformly-polarized over the detector/camera plane. If we assume that the speckle patterns are described by ergodic random processes, such that averages over the camera area are equal to averages over material translations, in hindsight the dramatic difference between these speckle patterns is somewhat intuitive. Statistically, depolarizing materials produce unpolarized speckle patterns. For depolarizing materials the relative polarization state (which in the video appears as relative irradiance) between two pixels varies randomly between different PSG and PSA states (from frame to frame in the video.) For depolarizing materials, solving the matrix equation (Eq. 2.7) therefore provides no more information than is present in a single frame, and results in noise amplification since in no norm are the condition numbers small enough that the error is propagated in a 1:1 ratio. What this implies is that any speckle noise in the initial measurement of \mathbf{I} for a depolarizing material is amplified when calculating \mathbf{M} using Eq. 2.10 *irrespective of the angle set used*. For non-depolarizing materials, however, solving the matrix equation extracts additional information (or signal), namely the relative intensities between the frames, that is unavailable from a single intensity measurement, resulting in a Mueller-averaged SNR greater than the intensity SNR. The results shown in Fig. 8 are inherently linked to speckle correlations and should therefore hold for any spatial bandwidth.

We finally briefly consider speckle noise as resolved among the individual Mueller-matrix elements. Figure 9 shows the SNR over speckle of each element of the Mueller matrices due to titanium and Spectralon at bandwidth 3 mm^{-1} . For any material that is being identified via a polarization signature it is desirable to measure a Mueller matrix with high SNR, but as Fig. 9 shows, for these materials most of the “signal” is in the diagonal elements. There exist other

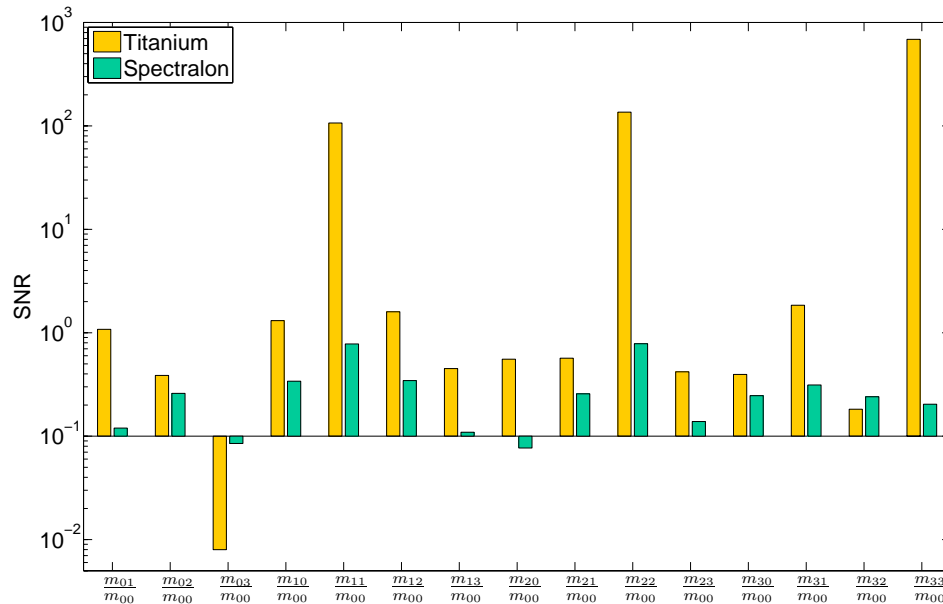


Fig. 9. SNR over speckle of the normalized Mueller matrix elements due to titanium and Spectralon at low bandwidth.

materials where most of the “signal” is in off-diagonal elements. These observations raise the question of whether we can minimize the noise in measurements of certain subsets of Mueller elements rather than the entire Mueller matrix as we have done in Section 2. Recent work in defining “partial condition numbers” [25] may be conducive to reducing noise in a specific subset of elements rather than the overall noise.

4. Conclusions

Mathematical analysis was carried out to find a bound on relative overall error for a DRR polarimeter using similar methodology to Ambirajan and Look [4], and an analytic solution was found. This analysis was then used to numerically compute optimal angle sets in four common norms. We recommend using one of these optimal angle sets in DRR polarimeters since in nearly all cases examined experimentally the optimal angle sets significantly improved Mueller-averaged SNR as compared to a standard 22.5° angle set. In section 3.2 experimental data was reported for different materials and spatial bandwidths. This experimental data showed clear advantages of the optimal angle sets over the standard 22.5° angle set for the reduction of system noise. The reduction of speckle noise was found to strongly depend on the depolarization index of the material, with little reduction found for highly-depolarizing materials. The Mueller-averaged SNR over speckle was compared with the polarized-intensity SNR over speckle, theoretically in the limit of zero bandwidth and experimentally for the minimum polarimeter bandwidth. The Mueller-averaged SNR was found to be larger than the polarized-intensity SNR for non-depolarizing materials and smaller for depolarizing materials. Reduction of noise in particular elements of the Mueller matrix rather than the average Mueller matrix is an interesting area for future analysis and research, particularly since certain elements tend to contain most of the “signal.” Successful analysis would allow customization of noise-reduction algorithms to focus on the “signal” for a particular material.

Acknowledgments

Thanks to Tony Peredo at Textron for data collection and custom mount manufacture, Victor Gamiz and Nick Morley at AFRL/RD, and Scott Tyo at the University of Arizona. This research was funded by the US Air Force Research Laboratory under contract FA9451-04-C-0353.